crystals

MDPI

Article

Defect Structures of Rare Earth-Doped Lutetium Oxide and Impacts of Li Co-Dopant

Yanfeng Zhao, Alastair N. Cormack * and Yiquan Wu

Kazuo Inamori School of Engineering, New York State College of Ceramics, Alfred University, Alfred, NY 14802, USA; yz8@alfred.edu (Y.Z.); wuy@alfred.edu (Y.W.)
* Correspondence: cormack@alfred.edu

Abstract: Defect complexes consisting of point defects induced by the doping of rare earth elements (Nd, Er) into lutetium oxide (Lu_2O_3) host were investigated with respect to defect formation energies and defect configurations using atomistic simulations with General Utility Lattice Program (GULP). The site preferences of the substitutional point defects of the dopants and the occupation between the two available cationic sites, the 8b and 24d sites, were analyzed. Additionally, the impacts of Li on the doping of rare earth elements into Lu_2O_3 were revealed from the viewpoints of energy and structure. Dopant pairs in the nearest neighbor configurations (8b + 8b), (8b + 24d), and (24d + 24d) were considered. The results contribute to the understanding of structures of defects in rare earth-doped Lu_2O_3.

Keywords: optical materials; atomistic simulation; point defect; rare earth dopant; lutetium oxide

1. Introduction

Oxides with cubic crystal structures have been of great research interest in the last two decades. Lutetium oxide (Lu_2O_3), with a C-type rare earth crystal structure (the bixbyite structure), is one of them. Properties such as high melting point, wide band gap, high density, and good thermal conductivity make it a good candidate as a solid-state laser host [1–3]. Nd (e.g., emission at around 1.06 μm) and Er (e.g., emission at around 1.5 and 3 μm) are recognized as ideal active laser ions for applications in the near and mid-infrared ranges. However, the main emission wavelengths may differ depending on the structure of the host. The optimal concentration of rare earth dopant in the popular laser hosts, such as Nd in YAG, is usually below 1.0 at%. One of the strong research interests in the bixbyite host is its potential capability of hosting high concentrations of rare earth elements, for example, 10 at % of Yb [4]. Experimental investigations have been continuously developing the processing, including powder synthesis and sintering, and optical properties, such as the analysis of optical spectra, to achieve high transparency. Despite the progress in fabrication routes and the well-established knowledge of the electronic structures of free rare earth ions, our understanding of the structure–property relationships in rare earth-doped bixbyite structure systems, especially with respect to optical properties, is still limited. For example, optical quenching occurs with high concentrations of doping, which limits the doping concentration to a certain level for an optimal emission intensity. According to the investigations of Nd-doped Lu_2O_3 by Goget [5], the emission cross-section (emission probability) of $^4F_{3/2} \rightarrow {}^4/I_{11/2}$ decreased as the concentration increased in the range of 1–5 at%. It was indicated that the dopant occupations of the two Lu sites influence the concentration measurement. Brunn [6] investigated Nd-doped single-crystal Lu_2O_3; the emission peak with the largest cross-section was at 1076 nm with 0.6% (1.71×10^{23} cm^{-3}) doping concentration. Strong luminescence quenching was observed in samples with higher concentrations (1%, 3%). From the viewpoint of the crystal structure, higher concentrations of dopants will induce more structural distortions. These findings reflected a strong correlation between optical properties and defect structures in Nd^{3+}:

check for updates

Citation: Zhao, Y.; Cormack, A.N.; Wu, Y. Defect Structures of Rare Earth-Doped Lutetium Oxide and Impacts of Li Co-Dopant. *Crystals* **2024**, *14*, 413. https://doi.org/10.3390/cryst14050413

Academic Editors: Weichao Bao and László Kovács

Received: 26 March 2024
Revised: 18 April 2024
Accepted: 25 April 2024
Published: 28 April 2024

Copyright: © 2024 by the authors. Licensee MDPI, Basel, Switzerland. This article is an open access article distributed under the terms and conditions of the Creative Commons Attribution (CC BY) license (https://creativecommons.org/licenses/by/4.0/).

Lu_2O_3. Luminescence quenching in Nd^{3+}: YAG has been attributed to several possible mechanisms of energy transfer and energy dissipation between nearby Nd dopants; for example, the cross-relaxation via the $^4I_{15/2}$ manifold [7,8]. The splitting of energy states due to an electric field acting upon the atom is called Stark splitting [7]. So, more specifically, the luminescence quenching is related to the electronic transitions between Stark levels of the manifolds. The crystal fields are different in different hosts, making the Stark splitting of rare earth dopants in YAG and Lu_2O_3 different; thus, their quenching mechanisms may be different. Defects induce perturbations to the crystal field and thus to the energy states of the dopants. Therefore, investigating the local structures of defects around the dopants is essential for achieving a better understanding of the optical quenching mechanisms. Zhou [9,10] fabricated a 3 at% Nd^{3+}: Lu_2O_3 ceramic using pressureless sintering with a reduced H_2 atmosphere. A high transparency of 75.5% (theoretical transparency is 81.7%) at 1080 nm was achieved. Luminescence peaks were found at 1079 nm. EXAFS (extended X-ray absorption fine structure) results indicated greater disorder in the sample with the higher luminescence intensity. However, the detailed local disordered structure was unclear due to the practical limitations of that characterization technique.

The synthesis of 1 mol% Er: Lu_2O_3 hollow microspheres was performed via a urea-based homogeneous precipitation method by Jia [11]. Three distinct up-conversion luminescence emissions were identified under 980 nm excitation. They were 540 nm, 566 nm, and 660 nm, corresponding to the electronic transitions of $^2H_{11/2} \rightarrow {}^4I_{15/2}$, $^4S_{3/2} \rightarrow {}^4I_{15/2}$, and $^4F_{9/2} \rightarrow {}^4I_{15/2}$, respectively. However, the site specification and partial contributions to the spectra from cationic sites remained unknown. Information about site preference is important for the analysis of spectra from the bixbyite structure, which offers more than one substitutional cation site for the dopants. Merkle [12] investigated the spectra of 0.22 at% Er^{3+}-doped Lu_2O_3; emissions at 1576 nm and 1601 nm were found to be promising for laser operation at cryogenic temperatures. Calculations of the cross-sections and radiative lifetime were performed based on two assumptions, which are difficult to verify experimentally. These were: (1) that Er^{3+} enters the 8b site without distortions; and (2) that it is random for Er^{3+} to enter 8b and 24d sites, and the concentration of 24d sites, which mainly contribute to the absorption spectra, is three-fourths of the total Er dopant concentration. So, information about the site occupations, local distortions, and respective spectra contributions is vital because they are the basis for evaluations of optical properties. The dependence of emission cross-section on the doping concentration was also observed in another work [13]. The sample with 11 at% Er doping concentration was found to possess the best laser performance. It was suggested that a homogeneous distribution of Er contributed to low quenching. Two mechanisms were proposed by Wang [14] for the up-conversion emissions (green band of $^4S_{3/2} \rightarrow {}^4I_{15/2}$ centers at 565 nm, red band of $^4F_{9/2} \rightarrow {}^4I_{15/2}$ centers at 660 nm) under 980 nm excitation. The main point of up-conversion is the excitation of electrons in excited levels to higher excited levels, either in a single Er^{3+} or between multiple Er^{3+}. In the latter case, energy transfer from one excited Er^{3+} to another is required. However, the question remains as to which Er^{3+} pair is involved in the energy transfer, 8b or 24d sites. Further investigations [15] found that the two main up-conversion emissions responded differently to increasing Er^{3+} doping concentrations. The green emission reached its maximum intensity at 3 at% (increased doping from 2 at% to 10 at%). Further increases in doping concentration, beyond 3 at%, decreased its emission intensity. Cross-relaxation was proposed to be responsible for the observed quenching phenomenon. Kränkel [3] discussed three mid-infrared laser emissions in Er-doped Lu_2O_3. The emission at 3 μm is related to two manifolds, $^4I_{11/2}$ and $^4I_{13/2}$. A relatively high doping concentration (>5%) was essential for laser gain from this electronic transition due to the influence of concentration on the lifetime of two terminal levels. It was mentioned that the disordered structure of the host would lead to changes in many aspects, such as absorption or emission line width, acceptance bandwidth, and even a decrease in thermal conductivity.

Co-doping with Li has been found to enhance the luminescence intensity of rare earth-doped oxides such as MgO. But the impact of co-doping Li in rare earth-doped

bixbyite Lu_2O_3 has received much less attention so far. Modulation of up-conversion luminescence by Li in multi-doping Nd/Yb/Er: Lu_2O_3 nano-powders was investigated by Liu et al. [16]. The doped samples were prepared using a chemical co-precipitation method. The energy transfers between dopants were proposed to be influenced by Li co-doping via the Foxter–Dexter relation [17] (the energy transfer probability between adjacent atoms being inversely proportional to the sixth power of interatomic distance). The substitution of Li on the Lu site was proposed to be more favorable for the intensity increase than Li interstitials by reducing the symmetry of the local crystal field. Co-doping with Li was also found to impact the optical properties of rare earth-doped Lu_2O_3 by Li et al. [18]. Detailed descriptions of the defect structures are necessary to better understand the role played by the presence of Li.

Above all, the local defect structures of optically active rare earth ions are closely related to the optical properties of the doped systems. However, characterizing the defects at the atomistic scale experimentally presents significant challenges. Therefore, the main objective of this paper is to investigate the point defect structures and the configurations of defect pairs and defect complexes in rare earth-doped (Nd, Er) Lu_2O_3 with and without co-doped Li using atomistic simulations.

2. Simulation Methodology

The program employed for the current simulations was the General Utility Lattice Program (GULP 6.0), which is based on classical force field methods. The static lattice method [19] was the methodology applied and it is outlined below.

The interactions between atoms are modelled by a series of functions with unique parameters depending on the nature of interactions between the different atoms. For materials that are considered mainly ionic, the lattice energy calculations include both long-range electrostatic interactions (the Coulomb term) and short-range interactions, namely the London interaction, which is known as the Van Der Waals interaction (or dispersion interaction, for historical reasons), and a repulsion term considering the Pauli exclusion rules. The lattice energy expressed by the three interaction terms is:

$$E_{Lattice} = \varphi_{Coulomb} + \varphi_{London} + \varphi_{Repulsion} \quad (1)$$

The repulsion term in the Born–Mayer exponential form can be combined with the dispersive term, which is induced by interactions between the instantaneous dipole moments and their induced instantaneous dipole moments. The combined term is known as the Buckingham potential, which was used in the current calculations. The two-body Buckingham potential is expressed as:

$$\varphi_{ij}^{Buckingham}(r_{ij}) = Aexp\left(-\frac{r_{ij}}{\rho}\right) - \frac{C_6}{r_{ij}^6} \quad (2)$$

A, ρ, and C_6 are the Buckingham parameters. It is computationally impractical to include interactions between all atoms in the solid as the number of atoms are on a scale of 10^{23} and Buckingham interations rapidly diminish with interatomic distance. Distance cut-offs were introduced to maintain a balance between efficiency and accuracy. Typically, a value of 5–10 Å is used. A cut-off distance of 10 Å and 12 Å were set for cation-oxygen and oxygen-oxygen potentials, respectively, in current simulations. The Ewald summation method was employed in the calculations of electrostatic interactions due to the slow convergence of $1/r$ summations. The arrangement of ions in the system was then determined by energy minimization processes with respect to all relevant structure factors, unit cell parameters, and atomic coordinates [19].

Atoms are treated as point ions, with the shell model proposed by Dick and Overhauser [13] being used to account for the polarizability of the ion. The shell model mimics the polarizability by defining an atom or ion as an entity consisting of a shell and a core

that interact through the spring constant K_{cs}. If the charges distributed on the shell of the ion are Q_s, the polarizability of the free ion can be expressed as:

$$\alpha = \frac{{Q_s}^2}{K_{cs}} \quad (3)$$

The sum of the core and shell charges is equal to the formal oxidation state of the ion. If all charges are on the core, the atom is considered to be unpolarizable. In the current simulations, the cationic cores possessed formal charges, and the charge distributions of O^{2-} were 0.869 e and −2.869 e on the core and shell, respectively. The K_{cs} of O^{2-} was 74.9.

The Mott–Littleton (ML) method, or the so-called two-region strategy, was used for calculations of defect formation energies. Atoms in the regions with different distances to the assigned defect center are treated differently. The ML method divides the whole system studied into two regions. Atoms in Region 1, closest to the defect, are treated explictly atomistically. Region 2 is divided into two. Region 2b is treated as a continuous dielectric medium. The energy was evaluated using classical continuum theory, and atomic displacements were determined by bulk polarization. Region 2a is an interface region that is treated both atomistically and as a dielectric continuum to provide consistency between Region 1 and Region 2b [19–21]. The radii of Region 1 and Region 2a were set to be 20 Å and 35 Å.

3. Results and Discussion

3.1. Intrinsic Point Defects in Pristine Lutetium Oxide

Pristine crystalline Lu_2O_3 under ambient condition possesses a stable C-type rare earth crystal structure with space group $Ia\bar{3}$ (No. 206), isomorphous with Y_2O_3, the bixbyite structure. The bixbyite crystal structure offers two types of cationic sites with different site symmetries: C_{3i} (Wyckoff position 8b) and C_2 (Wyckoff position 24d) [22]. The bixbyite structure can be seen as a pseudo-fluorite structure with ordered arrays of oxygen vacancies [23]. From the viewpoint of crystallography, the sixfold coordination of both types of Lu sites can be derived by removing two oxygen atoms from the eightfold coordination of cations in the fluorite structure [24], that is, removing two oxygen atoms from eight Lu (8b) centered cubes. These two coordination environments are differently distorted instead of being identically perfect. It causes the whole structure to be relatively more complex compared with simple cubic structures such as fluorite or rock salt. This way of observing the bixbyite structure provides convenience for locating potential interstitial sites within Lu_2O_3.

The Buckingham potentials used in calculations are listed in Table 1 [25,26]. The structural parameters of the current simulations are listed in Table 2. After bulk optimization, the relaxed lattice parameter is 10.285 Å (0.08 Å or 0.8%; smaller than the experimental result [22]), and the lattice energy is −138.273 eV. The relaxed crystal structure of the (a) unit cell and (b) octahedral coordination of 8b and 24d sites are shown in Figure 1.

Table 1. Buckingham potentials used in calculations.

Pairwise Interaction	A (eV)	ρ (Å)	C_6 (eV•Å^6)
Lu-O	1347.1	0.3430	0
O-O	22,764	0.1490	27.879
Nd-O	1379.9	0.3601	0
Li-O	235.1	0.3544	0
Er-O	1381.5	0.3492	0

Table 2. Optimized atomic positions of bixbyite Lu_2O_3.

Atom	Fractional Coordinate	Wyckoff Position	CN
Lu_1	(0.250, 0.250, 0.250)	8b	6
Lu_2	(0.471, 0.000, 0.250)	24d	6
O	(0.390, 0.152, 0.381)	48e	4

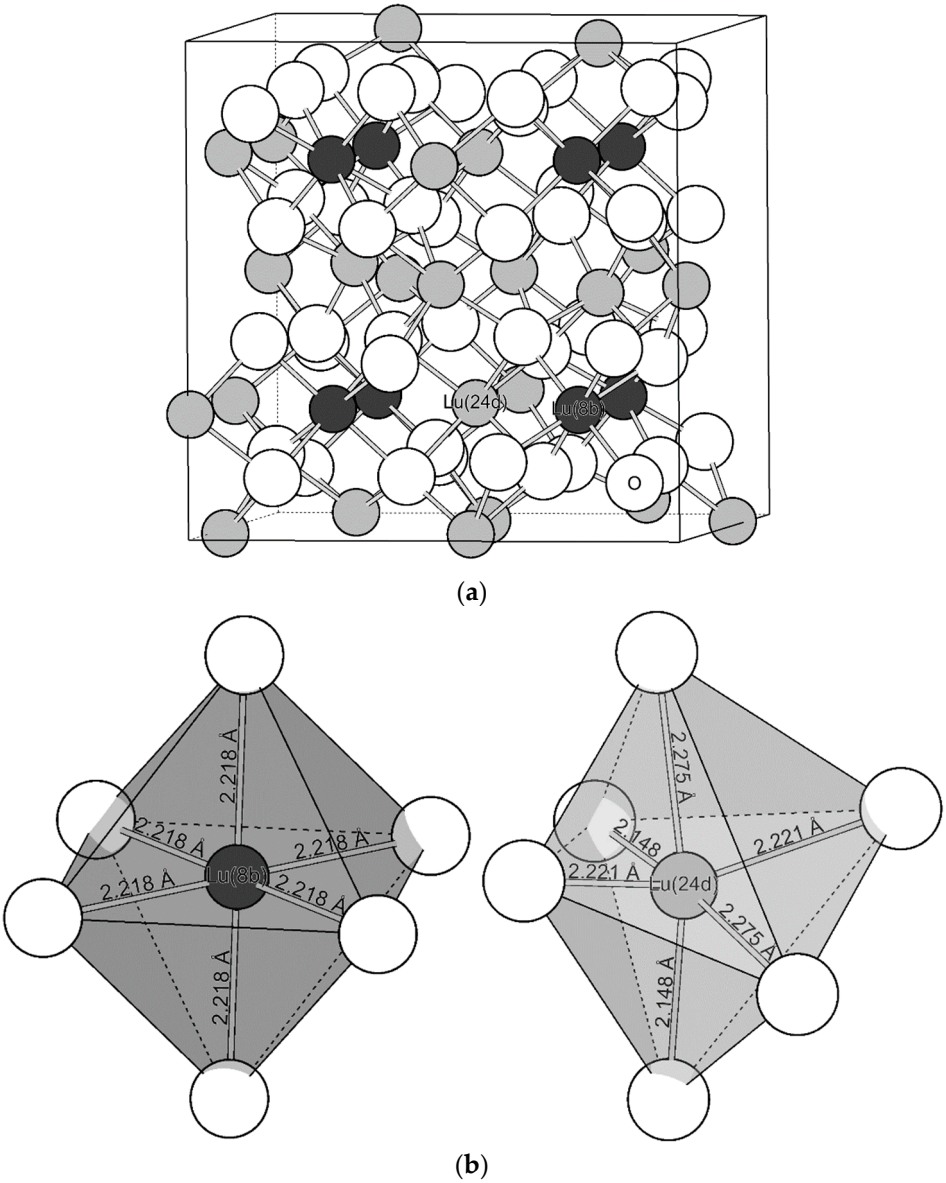

Figure 1. Relaxed crystal structure of Lu_2O_3. Dark grey: Lu 8b site. Light grey: Lu 24d site. White: O. (**a**) Lu_2O_3 unit cell and (**b**) coordination of Lu sites.

Intrinsic point defects in Lu_2O_3 include, using Kröger–Vink notation, vacancies $V_{Lu}^{'''}$, $V_O^{\bullet\bullet}$ and interstitials $Lu_i^{\bullet\bullet\bullet}$, $O_i^{''}$. In order to calculate the defect energies of defect complexes involving interstitials systematically, the coordinates of the available interstitial sites in the Lu_2O_3 unit cell are required. But these coordinates were not explicitly listed in the literature. So, a re-evaluation of potentially available interstitial sites was conducted based on the experimentally obtained crystal structure of Lu_2O_3 [22]. The crystal structure of Lu_2O_3 was observed in the following two parts from which potential interstitial sites were

identified. On the one hand, as shown in Figure 2a and as mentioned above, each Lu 8b site can be seen as being at the body center of a distorted cube, and the distribution of six coordinated oxygen atoms can be seen as removing two oxygen atoms from the eight body corners. All 48 oxygen atoms in the Lu_2O_3 unit cell can be seen to be in the eight distorted cubes. So, in total, there are 16 oxygen vacancies, i.e., potential interstitial sites, viewed from these Lu 8b-centered cubes. On the other hand, there is a fluorite type, a face-centered cube at the central part of the Lu_2O_3 unit cell, with eight Lu 8b sites at body corners and six Lu 24d sites at face centers. According to this center structure, another 13 potential interstitial points can be identified: they are 12 middle sites between adjacent Lu 8b sites and 1 at the body center, as shown in Figure 2b. These interstitial sites belong to the 16c, 24d, and 8a Wyckoff positions, respectively [27]. The fractional coordinates of the identified interstitial sites in the Lu_2O_3 unit cell are listed in Appendix A. An orthogonal view of those identified interstitial sites is shown in Figure 2c.

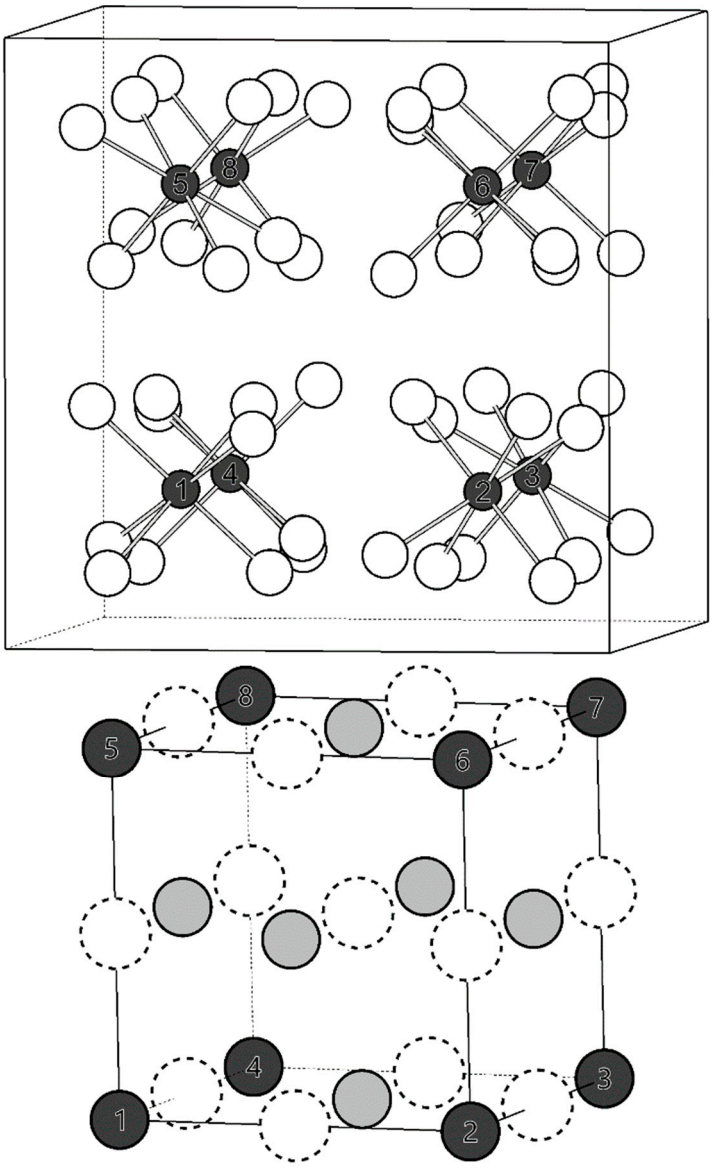

(**a**)

Figure 2. *Cont.*

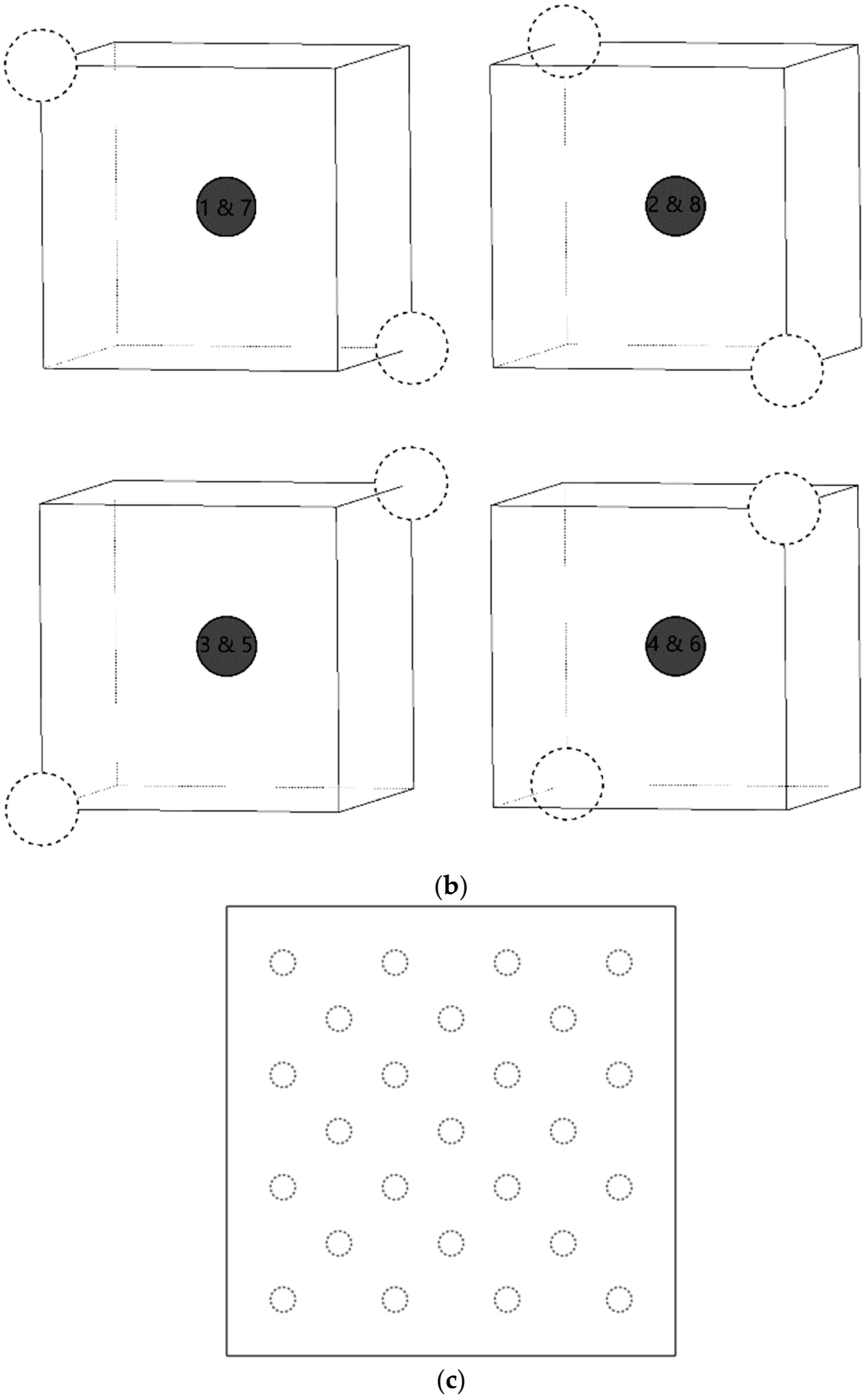

Figure 2. Identified interstitial sites in Lu_2O_3: (**a**) 16 ordered oxygen vacancies in 8 distorted cubes centered around Lu 8b sites; (**b**) 13 interstitial sites in the central fluorite-type cube; (**c**) interstitial sites viewed from <100>. Dark grey: Lu 8b site. Light grey: Lu 24d site. White: O. Dashed: potential interstitial site.

Results of the calculated defect formation energies of the four intrinsic point defects in pristine Lu_2O_3 are listed in Table 3.

Table 3. Defect formation energies in pristine Lu_2O_3.

Intrinsic Point Defect		Defect Formation Energy (eV)
$V_{Lu}^{'''}$	8b	50.014
	24d	50.709
$V_O^{\bullet\bullet}$	48e	20.933
$Lu_i^{\bullet\bullet\bullet}$	8a	−33.402
	24d	−32.669
	16c	−34.334
$O_i^{''}$	8a	−12.390
	24d	−11.016
	16c	−13.845

Using the lowest formation energy of each point defect, the Schottky and Frenkel defect energies (per defect) were obtained:

$$\begin{gathered} \text{Schottky}: \ \text{nil} \rightarrow 2V_{Lu}^{'''} + 3V_O^{\bullet\bullet} + Lu_2O_3 \ \Delta H = 4.910 \text{ eV} \\ \text{Frenkel Lu}: \ \text{nil} \rightarrow V_{Lu}^{'''} + Lu_i^{\bullet\bullet\bullet} \ \Delta H = 7.840 \text{ eV} \\ \text{Frenkel O}: \ \text{nil} \rightarrow V_O^{\bullet\bullet} + O_i^{''} \ \Delta H = 3.544 \text{ eV} \end{gathered} \quad (4)$$

Comparing the Schottky and Frenkel defect energies, the O Frenkel is the most favorable, consisting of one oxygen vacancy point defect and one oxygen interstitial point defect. This indicates that in undoped Lu_2O_3, intrinsically, there is a greater probability of finding O vacancies compensated by O interstitials compared with a Lu vacancy compensated by a Lu interstitial. At this point in the analysis, the point defects are isolated.

When point defects approach close to each other, they may associate with each other. The effective charges of defects may promote clustering, forming defect pairs or defect complexes. The association energy in the current context is defined as: $E_{association} = E_{complex} - \sum E_{isolated}$. So, the higher the association, the lower (more negative) the association energy, the lower the defect formation energy of the complex and the more favorable it is. Although Schottky disorder is less favorable than O Frenkel disorder, the association energies of the complexes were calculated systematically. Potential defect complexes include: $(V_{Lu}^{'''} + V_O^{\bullet\bullet})_{pair}$, $(2V_{Lu}^{'''} + V_O^{\bullet\bullet})_{complex}$, $(2V_O^{\bullet\bullet} + V_{Lu}^{'''})_{complex}$, $(3V_O^{\bullet\bullet} + V_{Lu}^{'''})_{complex}$, $(2V_O^{\bullet\bullet} + 2V_{Lu}^{'''})_{complex}$, and $(2V_{Lu}^{'''} + 3V_O^{\bullet\bullet})_{complex}$. All five defect complexes were considered, with 300 potential configurations being examined. The lowest association energies of each defect complex are shown in Table 4.

Table 4. Association energies of Schottky defect complexes in Lu_2O_3.

Defect	Effective Charge (e)	Association Energy (eV)
$(V_{Lu}^{'''} + V_O^{\bullet\bullet})_{pair}$	−1	−4.265
$(2V_{Lu}^{'''} + V_O^{\bullet\bullet})_{complex}$	−4	−5.402
$(2V_O^{\bullet\bullet} + V_{Lu}^{'''})_{complex}$	+1	−7.509
$(3V_O^{\bullet\bullet} + V_{Lu}^{'''})_{complex}$	+3	−8.638
$(2V_O^{\bullet\bullet} + 2V_{Lu}^{'''})_{complex}$	−2	−10.835
$(2V_{Lu}^{'''} + 3V_O^{\bullet\bullet})_{complex}$	0	−14.917

With the number of point defects increasing, a lower association energy is obtained. These results reveal a preference for clustering of the Schottky defects. The relaxed local

structure of Lu_2O_3 that contains one $(2V_{Lu}^{///} + 3V_O^{\bullet\bullet})_{complex}$ is shown in Figure 3. Due to the two oxygen vacancies of the cluster present, the seven neighboring Lu ions' coordination numbers were reduced by one. As a result, the coordination polyhedron changes from an octahedron to a distorted cuboid. The mean Lu-O distances of those cuboids are: 2.145 Å, 2.139 Å, 2.132 Å, 2.135 Å, 2.144 Å, 2.147 Å, and 2.146 Å. Ample void space emerges due to the clustering of these point defects, i.e., the vacancies. The dimensions of this void space concern the distance between these seven neighboring Lu ions. The minimum and maximum distances are 3.709 Å and 7.587 Å. This void space may be important for accommodating dopants of considerable size. If Schottky defect complexes are of high concentration, they will exert vital influences on physical properties, such as densities, and mechanical properties such as hardness and strength. It is noteworthy for studies related to dopants with a considerable size, as it is undoubtedly available space for interstitial point defects or even clusters.

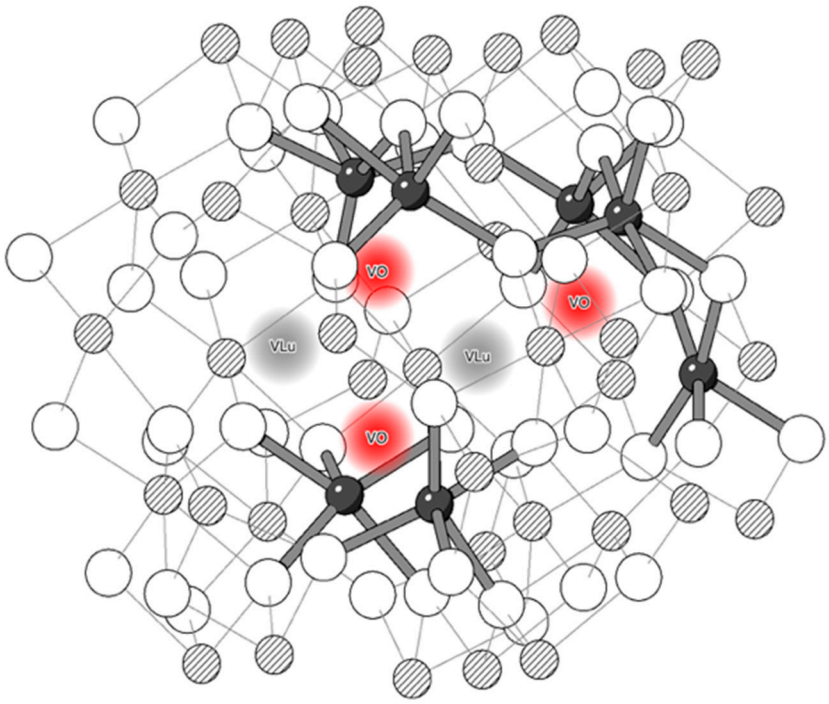

Figure 3. Configuration of $(2V_{Lu}^{///} + 3V_O^{\bullet\bullet})_{complex}$. Dark grey and striped: Lu atom. White: O atom.

3.2. Defect Structures of Rare Earth-Doped Lutetium Oxide

Neodymium (Nd) and erbium (Er) are the rare earth elements under current investigation. A primary problem of studying the doping mechanisms is to determine the preferential form of existence and preferential occupation site of the dopant in the host. As mentioned, there are plenty of potential interstitial sites in Lu_2O_3. Trivalent Nd and Er are isovalent with the Lu in the host, which means there is zero effective charge upon the substitution for Lu, and they possess similar ionic sizes. It is reasonable to assume a certain ease for them to be doped into the Lu_2O_3 host. Three sites were tested for interstitial Nd and Er: (0.625, 0.125, 0.375), (0.25, 0.50, 0.75), and (0.50, 0.50, 0.50). The lattice energies of Nd_2O_3, Er_2O_3, and Li_2O are −129.01 eV, −134.97 eV, and −29.67 eV after bulk optimizations when using the crystal structures from experimental results [28–33].

Table 5 lists the calculated defect formation energies of $Nd_i^{\bullet\bullet\bullet}$, $Nd_{Lu}^{\times}$, $Er_i^{\bullet\bullet\bullet}$, and $Er_{Lu}^{\times}$. It first shows that 16c is the preferable site for interstitial Nd and Er. Furthermore, both Nd and Er prefer 8b as the substitution site. This agrees with other simulation results, which reveal a relationship between preferential sites and ionic size [34]. However, the differences between the defect formation energies of substitutional point defects concerning the two Wyckoff positions are not significantly large. They are $\Delta E_1 = 0.108$ eV in Nd:

Lu_2O_3 and $\Delta E_2 = 0.041$ eV in Er: Lu_2O_3. Assuming that the energy differences are independent of temperature and constant entropy, statistically, the ratio of site occupation or concentration of 8b and 24d sites can be expressed by the Boltzmann distribution, where C is concentration: [35]

$$\frac{C_{8b}}{C_{24d} + C_{8b}} = \frac{\exp\left(-\frac{\Delta E}{kT}\right)}{\exp\left(-\frac{\Delta E}{kT}\right) + 3} \quad (5)$$

Table 5. Point defects in Nd (Er): Lu_2O_3.

Point Defect	Wyckoff Position	Defect Formation Energy (eV)
$Nd_{Lu}^{\times}$	8b	4.471
	24d	4.579
$Er_{Lu}^{\times}$	8b	1.832
	24d	1.873
$Nd_i^{\bullet\bullet\bullet}$	8a	−27.073
	24d	−26.183
	16c	−29.851
$Er_i^{\bullet\bullet\bullet}$	8a	−30.756
	24d	−29.947
	16c	−32.507

As a function of absolute temperature, from (5), the concentration ratio between the 8b and 24d sites can be straightforwardly derived as plotted in Figure 4. The temperature range shown in the plot is from 200 to 2150 K, that is, from room temperature to up to 1800 °C, a high temperature that might be reached during fabrication processes (e.g., sintering) of bulk polycrystalline ceramic materials.

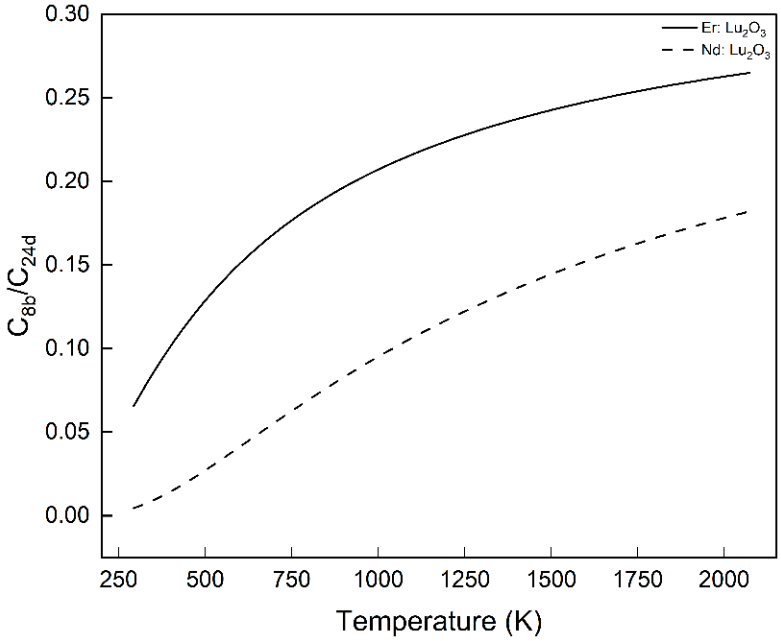

Figure 4. Concentration ratio of 8b and 24d sites in Nd: Lu_2O_3 and Er: Lu_2O_3.

Regarding the bixbyite structure, the quantity ratio between 8b and 24d sites in Lu_2O_3 is approximately 0.33. However, will dopants occupy those sites strictly according to the

quantity ratio of sites available? Our results show that the answer is negative. As shown, neither of the two dopants achieves the maximum ratio of 0.33. Within the temperature range considered, C_{8b}/C_{24d} reaches its maximum of 0.18 in Nd: Lu_2O_3 and 0.26 in Er: Lu_2O_3 at around 1800 °C. If the average sintering temperature is 1500 °C, then in Nd: Lu_2O_3, among all substituted sites, around 14% of them are 8b sites and 86% are 24d sites. In Er: Lu_2O_3, the concentration percentages are around 20% and 80% for 8b and 24d sites, respectively. Due to the smaller energy difference, at a specific temperature that provides sufficient energy for doping, more 8b sites are expected to be substituted in Er: Lu_2O_3 than Nd: Lu_2O_3, starting from an identical total doping quantity. From the viewpoint of energy, at 1500 °C, to reach a ratio of 0.33, ΔE is expected to be as small as 0.016 eV. Apparently, for Nd and Er, ΔE_1 and ΔE_2 are not small enough.

Putting the calculated point defect formation energies from Tables 3 and 5 into quasi-chemical reactions (in the Appendix A), the ones with the lowest enthalpy (per rare earth dopant) of Nd and Er dopants in substitutional and interstitial sites are:

$$Nd_2O_3 \overset{Lu_2O_3}{\rightarrow} 2Nd_{Lu}^{\times} + Lu_2O_3 \ \Delta H = -0.161 \text{ eV} \tag{6a}$$

$$Nd_2O_3 \overset{Lu_2O_3}{\rightarrow} 2Nd_i^{\bullet\bullet\bullet} + 3O_i'' \ \Delta H = 13.887 \text{ eV} \tag{6b}$$

$$Er_2O_3 \overset{Lu_2O_3}{\rightarrow} 2Er_{Lu}^{\times} + Lu_2O_3 \ \Delta H = 0.179 \text{ eV} \tag{6c}$$

$$Er_2O_3 \overset{Lu_2O_3}{\rightarrow} 2Er_i^{\bullet\bullet\bullet} + 3O_i'' \ \Delta H = 14.209 \text{ eV} \tag{6d}$$

The negative enthalpy in (6) indicates that the reaction is exothermal. Compared with the interstitial site, substitution is (much) more favorable. If interstitials with positive effective charges appear, O_i'' was found to be more favorable than V_{Lu}''' as the charge compensator.

To prove the preference for substitution from another aspect, the defect formation energies of $\left(Nd_i^{\bullet\bullet\bullet} + V_{Lu}'''\right)_{pair}$ and $\left(Er_i^{\bullet\bullet\bullet} + V_{Lu}'''\right)_{pair}$ were calculated. V_{Lu}''' was placed at (0.25, 0.25, 0.25), the 8b site, and all identified interstitial sites were tested for Nd and Er interstitials.

Figure 5 shows the results of the defect energies of defect pairs (a rare earth interstitial and a Lu vacancy) versus relaxed distance between the two point defects. At 0 Å, the interstitial rare earth dopant fills the Lu vacancy, becoming a substitutional defect. From 0′Å to around 4.5 Å, no data points are shown in the graph because all interstitial dopants initially placed in this range were relaxed to Lu sites. Nd interstitials were found to be directly relaxed to the (0.25, 0.25, 0.25) Lu site. For the Er interstitial, the surrounding Lu can be relaxed to the initial Lu vacancy. Then, the dopant interstitial fills the newly generated Lu vacancy, forming $Er_{Lu}^{\times}$ and leaving no vacancy at last. An example of this process is shown in Figure 6.

Initially, the Lu vacancy was placed at the 8b site (0.25, 0.25, 0.25) and the Er interstitial was placed at (0.75, 0.5, 0.25). After the energy minimization, the (0.25, 0.25, 0.25) position was filled by its neighboring Lu atom (Lu* as indicated), which was at a 24d site (0.53, 0.50, 0.25) initially. Alternatively, one could consider that the Lu vacancy moved to a neighboring 24d site. Then, the Er interstitial was found to occupy the initial position of Lu*, finally forming an $Er_{Lu}^{\times}$ point defect at the 24d site (0.53, 0.50, 0.25).

Another aspect worth investigating is the favorability of the configuration of dopant pairs. Experimental studies have shown that energy transfer between Eu dopants plays a significant role in the optical properties of Eu-doped bixbyite oxides [36]. For Nd-doped YAG, luminescence quenching phenomena were closely related to energy transfer and up/down conversions among adjacent Nd dopants. The mechanisms were discussed by Danielmeyer [8]. Calculations of the defect formation energies of dopant pairs will reveal which pairing configuration is more favorable for energy transfer, considering that the energy transfer probability is a function of interatomic distance [17]. A shorter distance indicates a greater probability of energy transferring between dopants. Three types of pairs

were considered: (8b + 8b), (24d + 24d), and (8b + 24d). A total of 54 configurations were examined for each dopant.

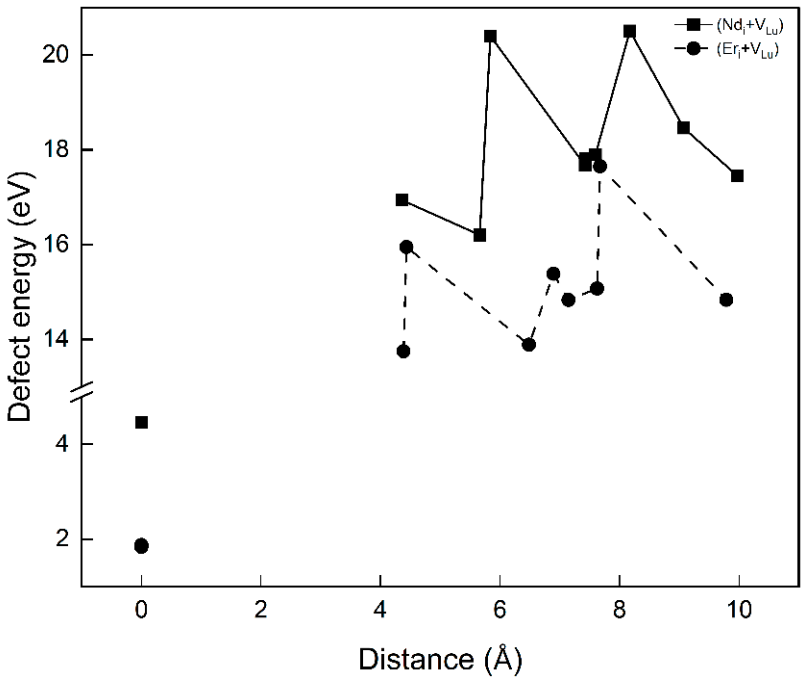

Figure 5. Defect energy between $V_{Lu}^{'''}$ and interstitial isovalent dopants.

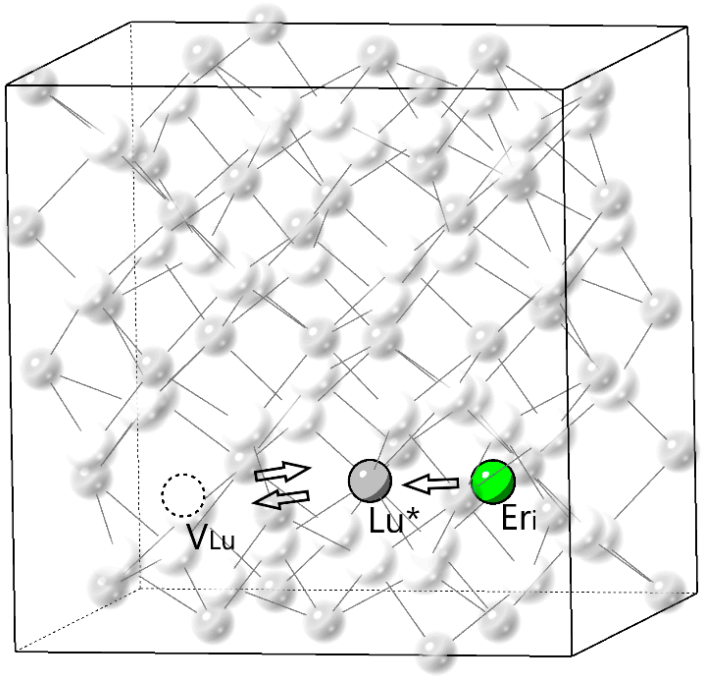

Figure 6. Illustration of an initially distant Er interstitial occupying a Lu vacancy. Fuzzy white: O atom; fuzzy light grey: Lu atom.

As shown in Figure 7, the defect formation energy depends on the sites (8b and 24d) occupied by the pair and the distance between two substitutional point defects. The dashed square highlights the lowest energy in each type of pair. The (8b + 8b) pair has the lowest defect formation energy, and the order of energetic favorability is (8b + 8b) > (8b + 24d) > (24d + 24d). This order is the same for Nd- and Er-doped systems. In an (8b + 8b) pair,

the most favorable interatomic distance is 8.907 Å, which is the third nearest neighbor (3rd NN) separation. Similarly, the third nearest neighbor configuration is also the most favored by the (8b + 24d) pair, with interatomic distances of 6.191 Å and 6.186 Å for Nd and Er dopants. Only (24d + 24d) most favors the nearest neighbor (NN) configuration, with interatomic distances of 3.524 Å and 3.478 Å for Nd and Er, respectively. According to the Foxter–Dexter relation [17], the energy transfer probability between adjacent atoms is inversely proportional to the sixth power of interatomic distance. The order of energy-transferring probability between two rare earth dopants among the three dopant pairs is then (24d + 24d) > (8b + 24d) > (8b + 8b). Table 6 lists the defect energies and inter-dopant distances of the NN and third NN configurations for the three types of pairs for both Nd and Er. When positioning two dopants in close proximity, such as in the nearest neighbor (NN) configuration of (8b + 24d) and (24d + 24d), Nd: Lu_2O_3 exhibits a higher degree of structural relaxation compared with Er: Lu_2O_3. The relaxed inter-dopant distances for the (8b + 24d) and (24d + 24d) NN configurations in Nd: Lu_2O_3 are 3.513 Å and 3.524 Å, respectively, which are greater than those in Er: Lu_2O_3, 3.466 Å and 3.478 Å. This discrepancy can be attributed to the larger ionic radius of Nd relative to Er. Note that the differences in the defect energies between the NN and the third NN configurations of (8b + 8b) and (8b + 24d) are on a scale of 0.001 eV in both Nd and Er doping systems, indicating that both configurations will appear in experimental practice. As for (24d + 24d), the configurations that are energetically close to the NN are the sixth or seventh NN. The favorability of NN configuration is relatively more significant in Nd- than Er-doped Lu_2O_3. Considering that there are twice as many Lu 24d sites than Lu 8b sites in the structure and considering the relative favorability of NN configuration, the energy transfer probability between two rare earth dopants in the (24d + 24d) pair may be the highest.

Table 6. Relaxed structures of $2Nd^{\times}_{Lu}$.

$2Nd^{\times}_{Lu}$	Configuration	Inter-Dopant Distance (Å)	Defect Energy (eV)
(8b + 8b)	NN	5.150	8.948
	3rd NN *	8.907	8.942
(8b + 24d)	NN	3.513	9.035
	3rd NN *	6.191	9.031
(24d + 24d)	NN *	3.524	9.144
$2Er^{\times}_{Lu}$	**Configuration**	**Inter-Dopant Distance (Å)**	**Defect Energy (eV)**
(8b + 8b)	NN	5.145	3.665
	3rd NN *	8.907	3.664
(8b + 24d)	NN	3.466	3.703
	3rd NN *	6.186	3.702
(24d + 24d)	NN *	3.478	3.744

* denotes the configuration of the lowest defect formation energy in each type of pair.

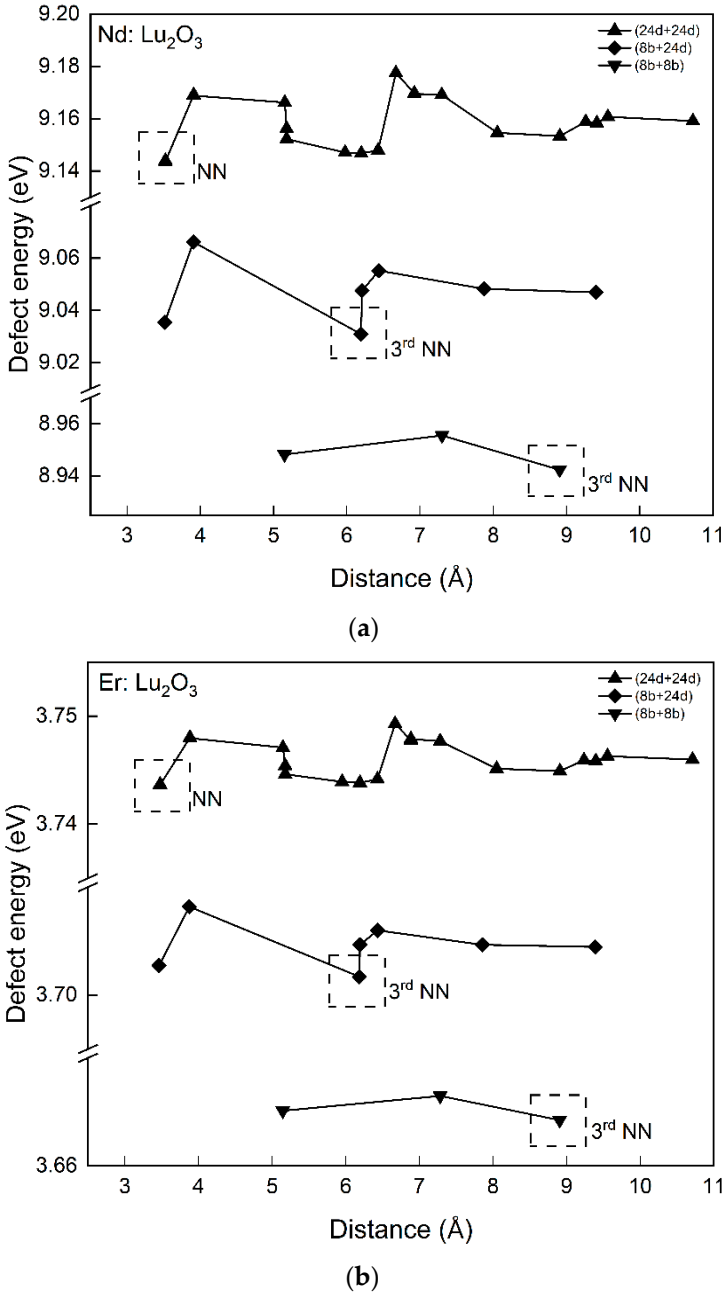

Figure 7. Variations of energy with distance between substitutional Nd or Er point defects: (**a**) Nd-doped; (**b**) Er-doped.

3.3. Defect Complexes Induced by Li Co-Doping

As noted in the Introduction, co-doping with Li has been experimentally shown to have an impact on optical properties. From the last section, it was shown that doping of Nd and Er into Lu_2O_3 requires relatively little energy. The substitution on the Lu site maintains the electroneutrality. No extra charge compensator is required. As for the co-doping of Li, the topics of interest are: (1) Does Li make it further easier for the doping of Nd and Er into the Lu_2O_3 host? (2) How will the inter-dopants distances change by co-doping Li? For the first question, comparing the enthalpy of the quasi-chemical reactions with and without Li will provide an answer. The second question requires calculations of the defect formation energies of the defect complexes containing the rare earth dopants and Li to determine the most favorable structures of the various defect complexes. With the incorporation of Li, two additional charged point defects $Li_i^{\bullet}$ and $Li_{Lu}^{//}$ may be introduced. Li favors the 8b and

24d sites as the substitutional and interstitial point defects; the defect formation energies of $Li_i^{\bullet}$ (8a) and $Li_{Lu}^{//}$ (24d) are −4.374 eV and 40.161 eV, respectively, as listed in Table 7.

Table 7. Defect formation energies of point defects of Li in Lu_2O_3.

Point Defect	Wyckoff Position	Defect Formation Energy (eV)
$Li_i^{\bullet}$	8a	−4.374
	24d	−4.916
	16c	−4.375
$Li_{Lu}^{//}$	8b	40.068
	24d	40.161

Possible quasi-chemical reactions in Li-doped Lu_2O_3 (per Li dopant) are shown in (7).

$$\frac{3}{2}Li_2O \overset{Lu_2O_3}{\rightarrow} 2Li_i^{\bullet} + Li_{Lu}^{//} + \frac{1}{2}Lu_2O_3 \ \Delta H = 1.868 \text{ eV} \quad (7a)$$

$$Li_2O \overset{Lu_2O_3}{\rightarrow} 2Li_i^{\bullet} + O_i^{//} \ \Delta H = 2.997 \text{ eV} \quad (7b)$$

$$\frac{3}{2}Li_2O \overset{Lu_2O_3}{\rightarrow} 3Li_i^{\bullet} + V_{Lu}^{///} + \frac{1}{2}Lu_2O_3 \ \Delta H = 3.545 \text{ eV} \quad (7c)$$

$$\frac{1}{2}Li_2O \overset{Lu_2O_3}{\rightarrow} Li_{Lu}^{//} + V_O^{\bullet\bullet} + \frac{1}{2}Lu_2O_3 \ \Delta H = 6.699 \text{ eV} \quad (7d)$$

$$\frac{3}{2}Li_2O \overset{Lu_2O_3}{\rightarrow} 3Li_{Lu}^{//} + 2Lu_i^{\bullet\bullet\bullet} + \frac{1}{2}Lu_2O_3 \ \Delta H = 8.968 \text{ eV} \quad (7e)$$

The most favorable way to accommodate Li in Lu_2O_3 is $Li_i^{\bullet}$ and $Li_{Lu}^{//}$ coexisting, as shown in reaction (7a). The two types of point defect of opposite effective charge can compensate each other. Consider $Li_i^{\bullet}$ and $Li_{Lu}^{//}$ separately; it can be found that $Li_i^{\bullet}$ is the more favorable point defect by comparing reactions (7b) and (7d), which are the reactions with the lowest enthalpies for $Li_i^{\bullet}$ and $Li_{Lu}^{//}$, respectively.

After introducing Li into Nd- and Er-doped Lu_2O_3, the lowest enthalpy reactions are:

$$Nd_2O_3 + \frac{3}{2}Li_2O \overset{Lu_2O_3}{\rightarrow} 2Nd_{Lu}^{\times} + 2Li_i^{\bullet} + Li_{Lu}^{//} + \frac{3}{2}Lu_2O_3 \ \Delta H = 2.641 \text{ eV} \quad (8a)$$

$$Er_2O_3 + \frac{3}{2}Li_2O \overset{Lu_2O_3}{\rightarrow} 2Er_{Lu}^{\times} + 2Li_i^{\bullet} + Li_{Lu}^{//} + \frac{3}{2}Lu_2O_3 \ \Delta H = 2.983\text{eV} \quad (8b)$$

By comparing (8a) and (8b) with (6a) and (6c), substitutional rare earth dopants do not benefit energetically from co-doping with Li, which only brings extra charged point defects that need to be compensated. Remember in reactions (6b) and (6d) that the favorable charge compensator for $Nd_i^{\bullet\bullet\bullet}$ and $Er_i^{\bullet\bullet\bullet}$ point defects is $O_i^{//}$. After introducing Li, $Li_{Lu}^{//}$ replaces $O_i^{//}$ as their favorable charge compensator:

$$Nd_2O_3 + \frac{3}{2}Li_2O \overset{Lu_2O_3}{\rightarrow} 2Nd_i^{\bullet\bullet\bullet} + 3Li_{Lu}^{//} + \frac{3}{2}Lu_2O_3 \ \Delta H = 13.303 \text{ eV}. \quad (9a)$$

$$Er_2O_3 + \frac{3}{2}Li_2O \overset{Lu_2O_3}{\rightarrow} 2Er_i^{\bullet\bullet\bullet} + 3Li_{Lu}^{//} + \frac{3}{2}Lu_2O_3 \ \Delta H = 13.629 \text{ eV}. \quad (9b)$$

By comparing reactions (9a) and (9b) with reactions (8a) and (8b), the advantage of substitutional sites to interstitial sites of rare earth dopants are not challenged by Li co-doping, as the energy required for interstitial point defects is still about four times higher than for substitutional point defects.

Considering the reactions (8), to determine which has the lowest enthalpy in Li-co-doped RE: Lu_2O_3 (RE = Nd, Er), it is necessary to consider the defect complex

$\left(2RE_{Lu}^{\times} + 2Li_i^{\bullet} + Li_{Lu}^{//}\right)_{complex}$. For $2RE_{Lu}^{\times}$, the nearest neighbor (NN) configurations were used. All three types of pairs were considered, (8b + 8b), (8b + 24d), and (24d + 24d). In searching for the most favorable structure of the defect complex, the point defects were placed and tested in the following way: The center of the dopant pair was fixed by placing two dopants first. Then, $Li_i^{\bullet}$, $Li_{Lu}^{//}$ were tested in a range from d_{min} to d_{max}. d_{max} is the distance between the pair center and the second nearest interstitial sites for $Li_i^{\bullet}$ and the second nearest Lu sites for $Li_{Lu}^{//}$. For each type of pair, the Wyckoff positions of the nearby sites tested for $Li_i^{\bullet}$ and $Li_{Lu}^{//}$ point defects are listed in Table 8. A total of 67 configurations of $\left(2RE_{Lu}^{\times} + 2Li_i^{\bullet} + Li_{Lu}^{//}\right)_{complex}$ were tested for each doping system.

Table 8. Wyckoff positions of the sites tested for $Li_i^{\bullet}$ and $Li_{Lu}^{//}$.

$2RE_{Lu}^{\times}$ in the Complex	Nearby Interstitial Sites Tested for $Li_i^{\bullet}$	Nearby Substitutional Sites for $Li_{Lu}^{//}$
NN (8b + 8b)	8a, 16c, 24d	24d
NN (8b + 24d)	16c, 24d	8b, 24d
NN (24d + 24d)	8a, 24d	24d

Table 9 lists the inter-dopants (the rare earth dopants) distances of the most favorable configurations of $\left(2Nd_{Lu}^{\times} + 2Li_i^{\bullet} + Li_{Lu}^{//}\right)_{complex}$ and $\left(2Er_{Lu}^{\times} + 2Li_i^{\bullet} + Li_{Lu}^{//}\right)_{complex}$, as well as the Wyckoff positions of the $Li_i^{\bullet}$ and $Li_{Lu}^{//}$ point defects in the defect complexes after relaxation.

Table 9. Relaxed structures of the $\left(2RE_{Lu}^{\times} + 2Li_i^{\bullet} + Li_{Lu}^{//}\right)_{complex}$.

$2Nd_{Lu}^{\times}$ in the Complex	Relaxed Wyckoff Positions of $Li_i^{\bullet}$	Relaxed Wyckoff Positions of $Li_{Lu}^{//}$	Relaxed Inter-Dopant Distance (Å)
NN (8b + 8b)	48e	48e	5.101
NN (8b + 24d)	48e	24d	3.560
NN (24d + 24d)	8a, 48e	48e	3.629
$2Er_{Lu}^{\times}$ in the Complex	Relaxed Wyckoff Positions of $Li_i^{\bullet}$	Relaxed Wyckoff Positions of $Li_{Lu}^{//}$	Relaxed Inter-Dopant Distance (Å)
NN (8b + 8b)	48e	48e	5.112
NN (8b + 24d)	48e	48e	3.411
NN (24d + 24d)	16c, 48e	16c	3.390

Investigating the effects of Li on the distances between the nearest neighbor dopants is important, because for each of the three types of pairs—(8b + 8b), (8b + 24d), and (24d + 24d)—the energy transfer probability is the highest in the nearest neighbor configurations. Comparing the inter-dopant distances of $2RE_{Lu}^{\times}$ from Table 6 and the $\left(2RE_{Lu}^{\times} + 2Li_i^{\bullet} + Li_{Lu}^{//}\right)_{complex}$ from Table 9, one finds that the inter-dopant distances change on a scale of 0.01–0.1 Å due to the incorporation of Li point defects near the rare earth dopant pairs. For $2Nd_{Lu}^{\times}$, nearby Li point defects cause the inter-dopant distance of NN (8b + 8b) to decrease. This effect is the same for the NN (8b + 8b) of $2Er_{Lu}^{\times}$. However, for NN (8b + 24d) and NN (24d + 24d) pairs, the effects of Li are opposite in $2Nd_{Lu}^{\times}$ and $2Er_{Lu}^{\times}$. The inter-dopant distances of NN (8b + 24d) and NN (24d + 24d) are increased in $2Nd_{Lu}^{\times}$ but decreased in $2Er_{Lu}^{\times}$ when co-doped with Li. From above, in Nd: Lu_2O_3, the

inter-dopant energy transfer is encouraged only in (8b + 8b) among the three types of NN configurations by Li co-doping. In Er: Lu_2O_3, inter-dopant energy transfer in all three types of NN configurations is encouraged by Li co-doping. So, the impact of Li on inter-dopant distance depends on the type of dopant and dopant pairs. But in both Nd- and Er-doped systems, Li has the least impact on the inter-dopant distance of the (8b + 8b) pair (a decrease of 1.0% and 0.6% in Nd- and Er-doped systems, respectively) and the most significant impact on the (24d + 24d) pair (an increase of 3.0% in the Nd-doped system; a decrease of 2.5% in the Er-doped system). These results are meaningful for the spectroscopic analysis of rare earth elements in Lu_2O_3 and provide a theoretical basis for co-doping with Li to control the concentration quenching of the rare earth elements in Lu_2O_3.

4. Conclusions

This paper investigated pristine and rare earth (Nd, Er)-doped Lu_2O_3 with respect to point defects and structures of defect complexes. The influence of Li as a co-dopant was considered. The defect formation energies were calculated, and the most energetically favorable defect structures were determined. In pristine Lu_2O_3, associations between the five individual point defects in the Schottky defect result in clustering, forming a local concentration of vacancies. According to the calculation results, the rare earth dopants, Nd and Er, energetically prefer the substitutional Lu sites compared with interstitial sites in the Lu_2O_3 host. This result supports the experimental characterization results, where the X-ray diffraction patterns of Nd: Lu_2O_3 [9] and Er: Lu_2O_3 [11,15] ceramic samples showed no impurity phase, indicating substitutions of Lu by Nd and Er dopants. The 8b site is more favorable than the 24d site for the substitutional Nd and Er point defects. Nevertheless, the energy difference is minor, on a scale of 0.01 eV–0.1 eV. The difference is smaller in Er: Lu_2O_3 than in Nd: Lu_2O_3. Attention was drawn to dopant pairs, considering the importance of the interatomic distance between dopants for energy transfer. Among the three types of dopant pairs, (8b + 8b), (8b + 24d), and (24d + 24d), the (8b + 8b) pair in the third nearest neighbor configuration possesses the lowest defect formation energy. Only the (24d + 24d) pair was found to most favor the nearest neighbor configuration. Therefore, energy transfer is predicted to occur with more probability in the (24d + 24d) configuration. $Li_{Lu}^{//}$ and $Li_i^{\bullet}$ are introduced by co-doping Li, and the energy required for the formation of charge compensators for these two charged point defects increases the enthalpy of doping Nd and Er into the Lu_2O_3 host. So, it is not energetically favorable to co-dope Li. Structurally, the effects of co-doping Li on the inter-dopant distances in the nearest neighbor configurations were found to be different in Nd and Er doping systems. Li has the least impact on the inter-dopant distances in the (8b + 8b) pair and a more significant impact on the (24d + 24d) pair.

The results can assist in the experimental analysis of the optical properties of rare earth-doped Lu_2O_3 and provide a basis to further investigate the concentration-induced luminescence quenching phenomena.

Author Contributions: Conceptualization, A.N.C. and Y.W.; investigation, Y.Z., A.N.C. and Y.W.; methodology, A.N.C.; supervision, A.N.C. and Y.W.; writing—original draft, Y.Z.; writing—review and editing, A.N.C. and Y.W. All authors have read and agreed to the published version of the manuscript.

Funding: This research received no external funding.

Data Availability Statement: The original contributions presented in the study are included in the article; further inquiries can be directed to the corresponding authors.

Acknowledgments: The formulation of the research topic in this work was crafted by Yiquan Wu and Alastair N. Cormack. We thank the Inamori School of Engineering at NYS College of Ceramics, Alfred University, for providing the computational resources for this work. Y.Z. would like to thank Alfred University for studentships.

Conflicts of Interest: The authors declare no conflicts of interest.

Appendix A

Table A1. Fractional coordinates of interstitial sites in Lu_2O_3 unit cell.

From 8 cation centered cubes	
Wyckoff position: 16c	
1. (0.625, 0.125, 0.375)	2. (0.875, 0.375, 0.125)
3. (0.125, 0.125, 0.125)	4. (0.375, 0.375, 0.375)
5. (0.875, 0.625, 0.375)	6. (0.625, 0.875, 0.125)
7. (0.375, 0.625, 0.125)	8. (0.125, 0.875, 0.375)
9. (0.375, 0.875, 0.625)	10. (0.125, 0.625, 0.875)
11. (0.625, 0.625, 0.625)	12. (0.875, 0.875, 0.875)
13. (0.375, 0.125, 0.875)	14. (0.125, 0.375, 0.625)
15. (0.625, 0.375, 0.875)	16. (0.875, 0.125, 0.625)
From central fluorite-type cube	
Wyckoff position: 24d	
17. (0.75, 0.5, 0.25)	18. (0.5, 0.75, 0.25)
19. (0.25, 0.5, 0.25)	20. (0.5, 0.25, 0.25)
21. (0.75, 0.25, 0.5)	22. (0.25, 0.25, 0.5)
23. (0.75, 0.75, 0.5)	24. (0.25, 0.75, 0.5)
25. (0.5, 0.75, 0.75)	26. (0.75, 0.5, 0.75)
27. (0.5, 0.25, 0.75)	28. (0.25, 0.5, 0.75)
Wyckoff position: 8a	
29. (0.5, 0.5, 0.5)	

Table A2. Quasi-chemical reactions of doping Nd into Lu_2O_3.

Reaction	ΔH Per Nd Dopant (eV)
$\frac{1}{2}Nd_2O_3 \overset{Lu_2O_3}{\rightarrow} Nd_i^{\bullet\bullet\bullet} + 3V_O^{\bullet\bullet} + 3V_{Lu}^{///} + \frac{3}{2}Lu_2O_3$	40.083
$\frac{1}{2}Nd_2O_3 \overset{Lu_2O_3}{\rightarrow} Nd_i^{\bullet\bullet\bullet} + V_O^{\bullet\bullet} + O_i^{//} + V_{Lu}^{///} + \frac{1}{2}Lu_2O_3$	22.619
$Nd_2O_3 \overset{Lu_2O_3}{\rightarrow} Nd_{Lu}^{\times} + Nd_i^{\bullet\bullet\bullet} + 3V_O^{\bullet\bullet} + 3V_{Lu}^{///} + 2Lu_2O_3$	19.961
$Nd_2O_3 \overset{Lu_2O_3}{\rightarrow} 2Nd_i^{\bullet\bullet\bullet} + V_O^{\bullet\bullet} + 4O_i^{//}$	17.430
$Nd_2O_3 \overset{Lu_2O_3}{\rightarrow} 2Nd_{Lu}^{\times} + 4V_O^{\bullet\bullet} + O_i^{//} + 2V_{Lu}^{///} + 2Lu_2O_3$	15.659
$Nd_2O_3 \overset{Lu_2O_3}{\rightarrow} 2Nd_i^{\bullet\bullet\bullet} + 2V_{Lu}^{///} + Lu_2O_3$	15.531
$\frac{3}{2}Nd_2O_3 \overset{Lu_2O_3}{\rightarrow} 3Nd_i^{\bullet\bullet\bullet} + 3O_i^{//} + V_{Lu}^{///} + \frac{1}{2}Lu_2O_3$	14.435
$Nd_2O_3 \overset{Lu_2O_3}{\rightarrow} 2Nd_i^{\bullet\bullet\bullet} + 3O_i^{//}$	13.887
$Nd_2O_3 \overset{Lu_2O_3}{\rightarrow} 2Nd_{Lu}^{\times} + 3V_O^{\bullet\bullet} + 2V_{Lu}^{///} + 2Lu_2O_3$	12.116
$\frac{3}{2}Nd_2O_3 \overset{Lu_2O_3}{\rightarrow} Nd_{Lu}^{\times} + 2Nd_i^{\bullet\bullet\bullet} + V_O^{\bullet\bullet} + 4O_i^{//} + \frac{1}{2}Lu_2O_3$	11.567
$Nd_2O_3 \overset{Lu_2O_3}{\rightarrow} Nd_{Lu}^{\times} + Nd_i^{\bullet\bullet\bullet} + V_O^{\bullet\bullet} + O_i^{//} + V_{Lu}^{///} + Lu_2O_3$	11.229
$2Nd_2O_3 \overset{Lu_2O_3}{\rightarrow} Nd_{Lu}^{\times} + 3Nd_i^{\bullet\bullet\bullet} + 3O_i^{//} + V_{Lu}^{///} + Lu_2O_3$	10.786
$\frac{3}{2}Nd_2O_3 \overset{Lu_2O_3}{\rightarrow} Nd_{Lu}^{\times} + 2Nd_i^{\bullet\bullet\bullet} + 3O_i^{//} + \frac{1}{2}Lu_2O_3$	9.204

Table A2. *Cont.*

Reaction	ΔH Per Nd Dopant (eV)
$Nd_2O_3 \overset{Lu_2O_3}{\rightarrow} Nd_{Lu}^{\times} + Nd_i^{\bullet\bullet\bullet} + V_{Lu}^{///} + Lu_2O_3$	7.685
$Nd_2O_3 \overset{Lu_2O_3}{\rightarrow} 2Nd_{Lu}^{\times} + V_O^{\bullet\bullet} + O_i^{//} + Lu_2O_3$	3.380
$Nd_2O_3 \overset{Lu_2O_3}{\rightarrow} 2Nd_{Lu}^{\times} + Lu_2O_3$	−0.161

Table A3. Quasi-chemical reactions of doping Er into Lu_2O_3.

Reaction	ΔH Per Er Dopant (eV)
$\frac{1}{2}Er_2O_3 \overset{Lu_2O_3}{\rightarrow} Er_i^{\bullet\bullet\bullet} + 3V_O^{\bullet\bullet} + 3V_{Lu}^{///} + \frac{3}{2}Lu_2O_3$	40.405
$\frac{1}{2}Er_2O_3 \overset{Lu_2O_3}{\rightarrow} Er_i^{\bullet\bullet\bullet} + V_O^{\bullet\bullet} + O_i^{//} + V_{Lu}^{///} + \frac{1}{2}Lu_2O_3$	22.941
$Er_2O_3 \overset{Lu_2O_3}{\rightarrow} Er_{Lu}^{\times} + Er_i^{\bullet\bullet\bullet} + 3V_O^{\bullet\bullet} + 3V_{Lu}^{///} + 2Lu_2O_3$	20.292
$Er_2O_3 \overset{Lu_2O_3}{\rightarrow} 2Er_i^{\bullet\bullet\bullet} + V_O^{\bullet\bullet} + 4O_i^{//}$	17.753
$Er_2O_3 \overset{Lu_2O_3}{\rightarrow} 2Er_{Lu}^{\times} + 4V_O^{\bullet\bullet} + O_i^{//} + 2V_{Lu}^{///} + 2Lu_2O_3$	15.998
$Er_2O_3 \overset{Lu_2O_3}{\rightarrow} 2Er_i^{\bullet\bullet\bullet} + 2V_{Lu}^{///} + Lu_2O_3$	15.854
$\frac{3}{2}Er_2O_3 \overset{Lu_2O_3}{\rightarrow} 3Er_i^{\bullet\bullet\bullet} + 3O_i^{//} + V_{Lu}^{///} + \frac{1}{2}Lu_2O_3$	14.757
$Er_2O_3 \overset{Lu_2O_3}{\rightarrow} 2Er_i^{\bullet\bullet\bullet} + 3O_i^{//}$	14.209
$Er_2O_3 \overset{Lu_2O_3}{\rightarrow} 2Er_{Lu}^{\times} + 3V_O^{\bullet\bullet} + 2V_{Lu}^{///} + 2Lu_2O_3$	12.454
$\frac{3}{2}Er_2O_3 \overset{Lu_2O_3}{\rightarrow} Er_{Lu}^{\times} + 2Er_i^{\bullet\bullet\bullet} + V_O^{\bullet\bullet} + 4O_i^{//} + \frac{1}{2}Lu_2O_3$	11.895
$Er_2O_3 \overset{Lu_2O_3}{\rightarrow} Er_{Lu}^{\times} + Er_i^{\bullet\bullet\bullet} + V_O^{\bullet\bullet} + O_i^{//} + V_{Lu}^{///} + Lu_2O_3$	11.560
$2Er_2O_3 \overset{Lu_2O_3}{\rightarrow} Er_{Lu}^{\times} + 3Er_i^{\bullet\bullet\bullet} + 3O_i^{//} + V_{Lu}^{///} + Lu_2O_3$	11.113
$\frac{3}{2}Er_2O_3 \overset{Lu_2O_3}{\rightarrow} Er_{Lu}^{\times} + 2Er_i^{\bullet\bullet\bullet} + 3O_i^{//} + \frac{1}{2}Lu_2O_3$	9.532
$Er_2O_3 \overset{Lu_2O_3}{\rightarrow} Er_{Lu}^{\times} + Er_i^{\bullet\bullet\bullet} + V_{Lu}^{///} + Lu_2O_3$	8.016
$Er_2O_3 \overset{Lu_2O_3}{\rightarrow} 2Er_{Lu}^{\times} + V_O^{\bullet\bullet} + O_i^{//} + Lu_2O_3$	3.722
$Er_2O_3 \overset{Lu_2O_3}{\rightarrow} 2Er_{Lu}^{\times} + Lu_2O_3$	0.179

References

1. Uehara, H.; Yasuhara, R.; Tokita, S.; Kawanaka, J.; Murakami, M.; Shimizu, S. Efficient continuous wave and quasi-continuous wave operation of a 28 μm Er: Lu_2O_3 ceramic laser. *Opt. Express* **2017**, *25*, 18677–18684. [CrossRef] [PubMed]
2. Lu, J.; Takaichi, K.; Uematsu, T.; Shirakawa, A.; Musha, M.; Ueda, K.; Yagi, H.; Yanagitani, T.; Kaminskii, A.A. Promising ceramic laser material: Highly transparent Nd^{3+}: Lu_2O_3 ceramic. *Appl. Phys. Lett.* **2002**, *81*, 4324–4326. [CrossRef]
3. Krankel, C. Rare-earth-doped sesquioxides for diode-pumped high-power lasers in the 1-, 2-, and 3-μm spectral range. *IEEE J. Sel. Top. Quantum Electron.* **2015**, *21*, 250–262. [CrossRef]
4. Liu, Z.; Ikesue, A.; Li, J. Research progress and prospects of rare-earth doped sesquioxide laser ceramics. *J. Eur. Ceram. Soc.* **2021**, *41*, 3895–3910. [CrossRef]
5. Goget, G.A.; Guyot, Y.; Guzik, M.; Boulon, G.; Ito, A.; Goto, T.; Yoshikawa, A.; Kikuchi, M. Nd^{3+}-doped Lu_2O_3 transparent sesquioxide ceramics elaborated by the Spark Plasma Sintering (SPS) method. Part 1: Structural, thermal conductivity and spectroscopic characterization. *Opt. Mater.* **2015**, *41*, 3–11. [CrossRef]
6. Von Brunn, P.; Heuer, A.M.; Fornasiero, L.; Huber, G.; Kränkel, C. Efficient laser operation of Nd^{3+}: Lu_2O_3 at various wavelengths between 917 nm and 1463 nm. *Laser Phys.* **2016**, *26*, 084003. [CrossRef]
7. Ikesue, A.; Aung, Y.L.; Lupei, V. *Ceramic Lasers*; Cambridge University Press: New York, NY, USA, 2013.
8. Danielmeyer, H.G.; Blätte, M.; Balmer, P. Fluorescence Quenching in Nd: YAG. *Appl. Phys.* **1973**, *1*, 269–274. [CrossRef]
9. Zhou, D.; Shi, Y.; Xie, J.; Ren, Y.; Yun, P. Fabrication and luminescent properties of Nd^{3+}-Doped Lu_2O_3 transparent ceramics by pressureless sintering. *J. Am. Ceram. Soc.* **2009**, *92*, 2182–2187. [CrossRef]
10. Zhou, D.; Ren, Y.; Xu, J.; Shi, Y.; Jiang, G.; Zhao, Z. Fine grained Nd^{3+}: Lu_2O_3 transparent ceramic with enhanced photoluminescence. *J. Eur. Ceram. Soc.* **2014**, *34*, 2035–2039. [CrossRef]

11. Jia, G.; You, H.; Zheng, Y.; Liu, K.; Guo, N.; Zhang, H. Synthesis and characterization of highly uniform Lu_2O_3: Ln^{3+} (Ln = Eu, Er, Yb) luminescent hollow microspheres. *CrystEngComm* **2010**, *12*, 2943–2948. [CrossRef]
12. Merkle, L.D.; Gabirielyan, N.T.; Kacik, N.J.; Sanamyan, T.; Zhang, H.; Yu, H.; Wang, J.; Dubinskii, M. Er: Lu_2O_3-Laser-related spectroscopy. *Opt. Mater. Express* **2013**, *3*, 1992. [CrossRef]
13. Uehara, H.; Tokita, S.; Kawanaka, J.; Konishi, D.; Murakami, M.; Shimizu, S.; Yasuhara, R. Optimization of laser emission at 28 μm by Er: Lu_2O_3 ceramics. *Opt. Express* **2018**, *26*, 3497. [CrossRef] [PubMed]
14. Wang, N.L.; Zhang, X.Y.; Wang, P.H. Fabrication and spectroscopic characterization of Er^{3+}: Lu_2O_3 transparent ceramics. *Mater. Lett.* **2013**, *94*, 5–7. [CrossRef]
15. Wang, N.; Zhang, X.; Wang, P. Synthesis of Er^{3+}: Lu_2O_3 nanopowders by carbonate co-precipitation process and fabrication of transparent ceramics. *J. Alloys Compd.* **2015**, *652*, 281–286. [CrossRef]
16. Liu, X.; Li, T.; Hu, W.; Zhao, P. Simultaneous size manipulation and up-conversion luminescence modulation of Lu_2O_3: $Nd^{3+}/Yb^{3+}/Er^{3+}$ nanospheres by Li^+ ion doping. *Mater. Res. Bull.* **2019**, *113*, 161–168. [CrossRef]
17. Dexter, D.L.; Schulman, J.H. Theory of concentration quenching in inorganic phosphors. *J. Chem. Phys.* **1954**, *22*, 1063–1070. [CrossRef]
18. Li, L.; Wei, X.; Cao, X.; Deng, K.; Chen, Q.; Chen, Y.; Guo, C.; Yin, M. Upconversion luminescence enhancement in Yb^{3+}/Tm^{3+}-codoped Lu_2O_3 nanocrystals induced by doping of Li^+ ions. *J. Nanosci. Nanotechnol.* **2011**, *11*, 9892–9898. [CrossRef]
19. Catlow, C.R.A.; Bell, R.G.; Gale, J.D. Computer modelling as a technique in materials chemistry. *J. Mater. Chem.* **1994**, *4*, 781. [CrossRef]
20. Du, J.; Cormack, A.N. (Eds.) *Atomistic Simulations of Glasses*; Wiley: Hoboken, NJ, USA, 2022.
21. Tilley, R.J.D. *Defects in Solids*; John Wiley & Sons: Hoboken, NJ, USA, 2008.
22. Guzik, M.; Pejchal, J.; Yoshikawa, A.; Ito, A.; Goto, T.; Siczek, M.; Lis, T.; Boulon, G. Structural investigations of Lu_2O_3 as single crystal and polycrystalline transparent ceramic. *Cryst. Growth Des.* **2014**, *14*, 3327–3334. [CrossRef]
23. Lee, D.; Gao, X.; Sun, L.; Jee, Y.; Poplawsky, J.; Farmer, T.O.; Fan, L.; Guo, E.; Lu, Q.; Heller, W.; et al. Colossal oxygen vacancy formation at a fluorite-bixbyite interface. *Nat. Commun.* **2020**, *11*, 1371. [CrossRef]
24. Hanic, F.; Hartmanova, M.; Aida, G.G.; Urusovskaya, A.A.; Bagdasarov, K.S. Real Structure of Undoped Y_2O_3 Single Crystals. *Acta Cryst. B* **1936**, *40*, 76–82. [CrossRef]
25. Lewis, G.V.; Catlow, C.R.A. Potential models for ionic oxides. *J. Phys. C Solid State Phys.* **1985**, *18*, 1149. [CrossRef]
26. Zhao, Y.; Cormack, A.N.; Wu, Y. Atomistic simulations of defect structures in rare earth doped magnesium oxide. *Crystals* **2024**, *14*, 384. [CrossRef]
27. Aroyo, M.; Perez, J.M.; Capillas, C.; Kroumova, E.; Ivantchev, S.; Madariaga, G.; Kirov, A.; Wondratschek, H. Bilbao Crystallographic Server: I. Databases and crystallographic computing programs. *Zeitschrift Kristallographie* **2006**, *221*, 15–27. [CrossRef]
28. Faucher, M.; Pannetier, J.; Charreire, Y.; Caro, P. X-ray structure analysis and molecular conformation of tert-butyloxycarbonyl-L-prolylproline (Boo-Pro-Pro): Errata. Refinement of the $Nd_2O_3$and Nd_2O_2S structures at 4 K. *Acta Cryst. B* **1982**, *38*, 344. [CrossRef]
29. Islam, M.M.; Bredow, T.; Minot, C. Theoretical analysis of structural, energetic, electronic, and defect properties of Li_2O. *J. Phys. Chem. B* **2006**, *110*, 9413–9420. [CrossRef] [PubMed]
30. Goel, P.; Choudhury, N.; Chaplot, S.L. Superionic behavior of lithium oxide Li_2O: A lattice dynamics and molecular dynamics study. *Phys. Rev. B* **2004**, *70*, 174307. [CrossRef]
31. Ohno, H.; Konishi, S.; Noda, K.; Takeshita, H.; Yoshida, H.; Watanabe, H.; Matsuo, T. Conductivities of a sintered pellet and a single crystal of Li_2O. *J. Nucl. Mater.* **1983**, *118*, 242–247. [CrossRef]
32. Guo, Q.; Zhao, Y.; Jiang, C.; Mao, W.L.; Wang, Z.; Zhang, J.; Wang, Y. Pressure-induced cubic to monoclinic phase transformation in erbium sesquioxide Er_2O_3. *Inorg. Chem.* **2007**, *46*, 6164–6169. [CrossRef]
33. Berard, M.F.; Wilder, D.R. Cation Self-Diffusion in Polycrystalline Y_2O_3 and Er_2O_3. *J. Am. Ceram. Soc.* **1969**, *52*, 85–88. [CrossRef]
34. Levy, M.R.; Stanek, C.R.; Chroneos, A.; Grimes, R.W. Defect chemistry of doped bixbyite oxides. *Solid State Sci.* **2007**, *9*, 588–593. [CrossRef]
35. Stanek, C.R.; McClellan, K.J.; Uberuaga, B.P.; Sickafus, K.E.; Levy, M.R.; Grimes, R.W. Determining the site preference of trivalent dopants in bixbyite sesquioxides by atomic-scale simulations. *Phys. Rev. B Condens. Matter. Mater. Phys.* **2007**, *75*, 134101. [CrossRef]
36. Buijs, M.; Meyerink, A.; Blasse, G. Energy transfer between Eu^{3+} ions in a lattice with two different crystallographic sites: Y_2O_3: Eu^{3+}, Gd_2O_3: Eu^{3+} and Eu_2O_3. *J. Lumin.* **1987**, *37*, 9–20. [CrossRef]

Disclaimer/Publisher's Note: The statements, opinions and data contained in all publications are solely those of the individual author(s) and contributor(s) and not of MDPI and/or the editor(s). MDPI and/or the editor(s) disclaim responsibility for any injury to people or property resulting from any ideas, methods, instructions or products referred to in the content.